J. Fluid Mech. (1983), *vol.* 136, *pp.* 291–319
Printed in Great Britain

A shear-flow instability in a circular geometry

By M. RABAUD AND Y. COUDER

Groupe de Physique des Solides de l'Ecole Normale Supérieure,
24 rue Lhomond, 75005 Paris, France

(Received 26 October 1982 and in revised form 15 March 1983)

A circular shear zone is created in a thin layer of fluid. The Kelvin–Helmholtz instability induces regular, steady patterns of m vortices. The experimental conditions are such that neither the centrifugal nor the Coriolis forces play a role in the motion. The state of the flow is defined by a Reynolds number, the value of which is controlled by the imposed velocities. The pattern of vortices can be characterized by its wavevector k or by m, the order of its symmetry. As k is quantized, its evolution, due to an increase or a decrease of the controlled stress, leads to transitions between patterns of different m. The transitory states between different symmetries are investigated. The experiments are performed with a soap film which provides a new type of visualization of an air flow.

1. Introduction

In this study, we present an experimental configuration where steady modes of the shear-flow instability are obtained in a circular geometry.

The instability that affects a detached shear zone (known as the Kelvin–Helmholtz instability in the case of a discontinuous velocity field) has been widely studied recently (Winant & Browand 1974; Roshko 1976; and references therein). In the usual experimental set-up, a plane detached shear layer is created by bringing together two streams of fluids of different velocities. The end of a splitter plate, where the two fluids meet, marks the origin of the shear layer. The thickness of this layer increases with the distance; thus the Reynolds number based on the velocity difference and the mixing-layer thickness grows continuously with the downstream distance from the origin. The transverse velocity profile has an inflexion point so that there is a plane zone where vorticity is maximum. This plane is unstable, small disturbances near the origin grow into waves, then into a regular line of vortices, which, in turn, undergo pairing to give rise to large structures in the turbulent regime far from the origin. Spatial and temporal evolution have to be taken into account to describe the evolution of the flow.

Less attention has been paid to the possibility of the Kelvin–Helmholtz instability leading to steady regimes in the case of a cylindrical detached shear zone.

Regular patterns of peripheral vortices in a cylindrical case were first observed by Weske & Rankin (1963). They created a columnar vortex and observed that there was a region around the core where the presence of peripheral vorticity gave rise to a transient periodic concentration of vorticity.

The problem of creating a permanent cylindrical shear layer is difficult as this layer must satisfy two conditions in order to be affected by the Kelvin–Helmholtz instability. The velocity profile should have an inflexion point and the flow should be two-dimensional in planes perpendicular to the rotation axis. As we will see, it

is only if the second condition is satisfied that neither the centrifugal nor the Coriolis forces will affect the flow.

The difficulty in meeting both conditions is illustrated in the following summary of the results obtained in two classical cylindrical geometries.

In the Couette configuration, a fluid is enclosed between two long coaxial cylinders rotating at different rates. The fluid is submitted to a shear constraint. But the boundary conditions on walls perpendicular to the velocity gradient create a velocity profile which does not have an inflexion point. The Kelvin–Helmholtz instability cannot appear. While the basic motion is two-dimensional, at the extremities of the cylinders there exists a three-dimensional flow where the centrifugal force becomes the destabilizing factor. A structure of piled-up tori then spreads from the ends into all the cell. This flow breaks down the translational invariance first, and only for stronger stresses will it break the continuous axial symmetry when the wavy modes appear. However, patterns of rollers with their axes parallel to the rotation axis were observed in the Couette geometry by Coles (1965). They corresponded to transitory states when sudden starts and stops of the rotation of the outer cylinder created an inflexion in the radial profile of the velocity.

In the geometry introduced by Hide & Titman (1967) a disk is placed in the centre of a cylindrical tank filled with fluid. The tank and the disk rotate respectively at Ω_0 and $\Omega_0(1+\epsilon)$ around their common axis. When the mean rotation is high, a Taylor column, rotating at the mean velocity, develops on both sides of the disk. The Stewartson layer that separates this column from the rest of the fluid is a detached shear layer. Non-axisymmetric patterns of m waves were observed in planes perpendicular to the rotation axis above the plane of the disk. However, the difference between the instabilities observed for positive and negative values of the constraint ϵ shows that it is not a simple Kelvin–Helmholtz instability. In the observation planes, a vertical component of the velocity in the Stewartson layer is due to a general circulation in the cell. The Rossby and Ekmann numbers being very small and the flow being three-dimensional, the Coriolis force plays an important role in the amplification or the inhibition of the vortices. This experiment gave rise to theoretical calculations by Busse (1968) and Siegmann (1974).

In our experimental cell, the flow is induced by walls moving perpendicular to the rotation axis. In order to create a circular shear zone, the fluid is enclosed in a very short and broad cylinder, the top and bottom of which are both formed of disks of radius R_1 rotating at an angular velocity Ω_1 surrounded by an annulus rotating at Ω_2. The thickness e of the cell is small, $e \ll R_1$, so the friction on the walls drives the fluid into two concentric solid rotations with angular velocities Ω_1 and Ω_2 separated by a shear zone with an inflexion in its velocity profile. For low values of the shear stress, an axisymmetric flow is stabilized by viscosity. The symmetry of the cell is such that the motion in its median plane can be considered as quasi-two-dimensional and is not affected by the three-dimensional recirculation that exists elsewhere. As the shear-zone width is maximum in this plane, the first instability is then a Kelvin–Helmholtz one which starts growing in that region. It produces in the circular zone a pattern of m_c regularly spaced vortices that is characterized by its wavevector k_c. This pattern is stable throughout a certain range of values of the stress. A further increase creates a situation where the mode is no longer stable. Global oscillations, with subharmonic spatial periodicity, will be observed before pairing of vortices, rolling around each other, leads to the coalescence of one or several pairs. The pattern then becomes a regular $m_c - p$ shape with a smaller wavevector.

In our experiment, in contrast with the linear case, the stress can also be reduced

and reverse transitions $m' \rightarrow m$ ($m > m'$) are observed so that the complete range of stability of a given wave pattern can be explored.

Finally, the patterns of vortices are observed using a visualization technique introduced in a preliminary work (Couder 1981). We insert a soap film in the median plane of the cell. Interference fringes produced in the film correspond to the flow lines. A discussion of this technique is given in the Appendix.

2. The experimental apparatus

2.1. *The cell*

The fluid used in our experiment was air. The experimental cell (figure 1*a*) was a vertical cylinder of radius R_2 and height $e \ll R_2$, closed at the bottom and the top by circular plates, the central parts of which were independent disks each of radius R_1. These disks were rotated at an angular velocity Ω_1 while the rest of the cell was rotated at Ω_2 around the same axis.

Figure 1 (*b*) shows a detailed drawing of the apparatus, the principle of which is sketched in figure 1 (*a*). For visualization of the flow, the top parts of the cell were made of Perspex. A cylindrical axis of radius R_0 passing through the cell fixed the top central disk to the bottom one. This axis did not disturb the flow insofar that there was a solid-body rotation of the fluid near the centre.

Two superposed cylinders, each of height $\frac{1}{2}e$, composed the lateral vertical walls. The lower cylinder had a rim on which a horizontal soap film could be stretched before the beginning of the experiment. A small rim isolated the film from the central axis.

The cell was designed in such a way that by changing some of its parts we could change the dimensions R_1 and e. The following values were used in the present set of experiments:

$$R_1 = 2.1 \quad \text{or} \quad 3.0 \quad \text{or} \quad 4.0 \text{ cm};$$

$$e = 0.2 \quad \text{or} \quad 0.3 \quad \text{or} \quad 0.5 \quad \text{or} \quad 0.9 \text{ cm};$$

$$R_2 = 5.1 \text{ cm} \quad \text{and} \quad R_0 = 0.8 \text{ cm}.$$

The gap ϵ between the rotating disks R_1 and the surrounding annuli was as small as practicable $\epsilon \sim 0.01$ cm.

The rotating parts of the apparatus were driven through two belt transmissions by two independent d.c. voltage-regulated motors with a typical range of frequencies $0.2 \text{ Hz} < f < 8 \text{ Hz}$ and an uncertainty of 0.03 Hz. Both angular velocities could be linearly increased or decreased with accelerations ranging from 6×10^{-3} Hz/s to 0.2 Hz/s.

Frequency measurements with chopped light beams provided excellent precision for the determination of the velocities.

2.2. *Visualization technique*

The flow in the cell was mainly observed from above. Photographs were taken, and a videotape recorder was also used to analyse the rapid phenomena such as the transition between modes. Whenever a large value of the rotation velocity Ω_w of the pattern made its direct visual observation difficult, we used a rotoscope to get a stationary image. This was provided by means of a dove prism rotating at $\frac{1}{2}\Omega_w$ around the axis of the system.

We used two different visualization techniques, one based on the conventional smoke emission, and one using the interference fringes produced in a soap film.

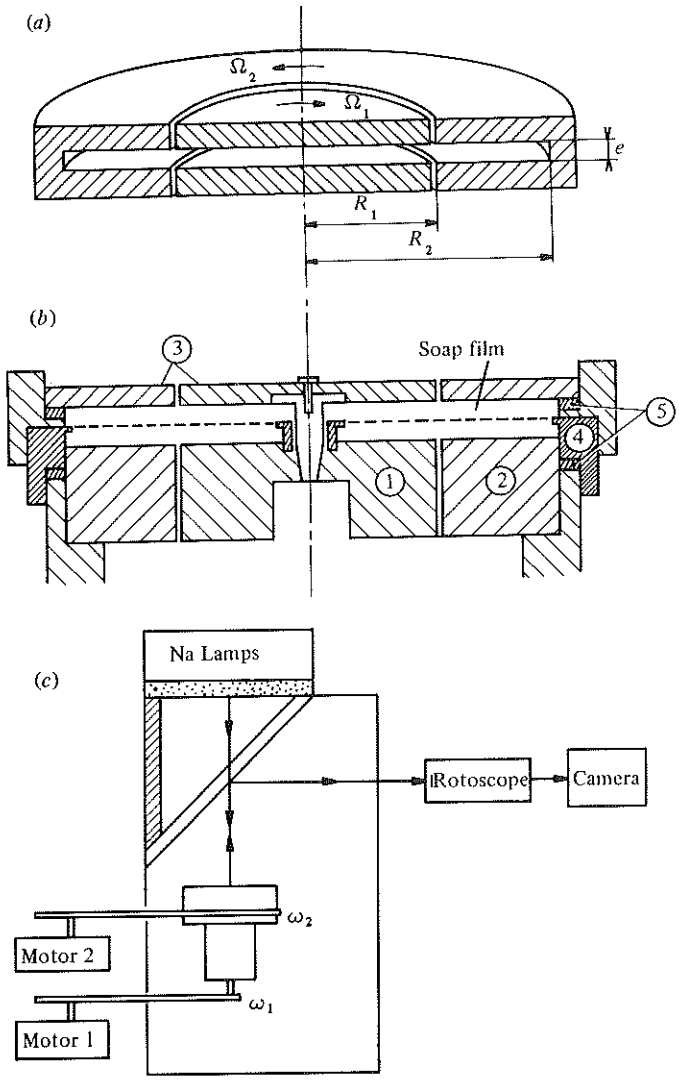

FIGURE 1. The experimental apparatus. (*a*) Sketch of a section across the ideal cell. (*b*) The practical design of the cell, showing: (1) the lower central disk; (2) the lower external annulus; (3) the corresponding top parts made out of Perspex. The cylinders (4) have rims on which the soap film (represented by the dotted line) is stretched. The thickness of the cell can be chosen by changing the rings (5). (*c*) General sketch showing the apparatus enclosed in a Perspex box with a 45° semireflecting mirror for normal illumination and observation.

The smoke technique served two purposes: to check the result obtained with the film and to visualize the eventual three-dimensional structure of some flows. Droplets of ammonia solution and hydrochloric acid were deposited on the bottom of the cell before the beginning of the experiment. The rotation of the disk mixed the fumes and created a dense ammonium chloride smoke which was illuminated by a lateral white light source. The best visualization was obtained at the beginning of the emission of smoke when streak lines were clearly observed.

The soap film

A horizontal soap film could be stretched in the median plane of the cell before the beginning of the experiment. We used a 0.5 % solution of a commercial liquid soap which was a mixture of sodium lauryl sulphate and sodium dodecyl benzene sulphate. An addition of 5 % glycerol produced more-stable films. The experiments were performed in a humid atmosphere so as to minimize evaporation. In practice, the same film could be used more than 1 h before breaking or excessive thinning.

An extended sodium light source lit the cell from above through a 45° semireflecting mirror (figure 1*c*) which permitted normal illumination and observation of the film.

In the Appendix, we recall a few properties of the soap films along with a discussion of their role in the present experiment. The following conclusions can be drawn on how the film affects the motion and how it provides a visualization of the flow.

The film is plane throughout the experiment, the curvature due to its weight is negligible and the capillary forces resist deformation. It is easily set into motion by air flows parallel to its surface and then behaves like a plane liquid with a kinematic viscosity $\nu \approx 5 \times 10^{-2}$ St smaller than the viscosity of air.

The air flow in the median plane of the cell is two-dimensional. The introduction of a soap film in that plane does not disturb the flow and only produces a slight decrease of the effective kinematic viscosity of the fluid contained in the cell.

During the experiment, the film thins down constantly, though very slowly, by a drainage mechanism mainly due to local centrifugal forces. When illuminated with monochromatic light, the patterns of interference fringes corresponding to lines of equal thickness give a good visualization of the flow lines.

3. General description of the experimental results

We will describe the phenomena as they can be observed on a soap film. For low values of both rotation velocities Ω_1 and Ω_2, the central part of the film moves with solid-body rotation at Ω_1 and the external part at Ω_2, and a circular zone of shear stress separates the two areas. The action of centrifugal forces slowly thins down the film, and concentric circular fringes are observed.

For a value $\Delta\Omega_c$ of the velocity difference $|\Omega_2 - \Omega_1|$, an oscillation of the fringes located in the shear zone amplifies suddenly into a regular mode of m_c vortices of elliptic shape (figures 2 and 3). In these zones, the rotation of the fluid of the liquid film creates elliptic fringes due to local centrifugation. The structure of m_c vortices rotates as a whole at an angular velocity that we will call Ω_w.

The same experiment can be repeated, in the absence of a film, smoke being emitted near the gap between the central disk and the surrounding annulus. At about the same value of $\Delta\Omega_c$, the pattern of m_c vortices appear. Each vortex has a vertical axis. The size of its transverse section is maximum in the median plane of the cell and decreases along the axis on both sides toward the slits.

The values of $\Delta\Omega_c$ depend on the radius R_1 and the thickness e, and will be discussed in §4.1, together with the selection rules for the value of m_c. An interpretation of the existence and value of the threshold will be given in §4.2.

The m_c mode is stable through a range of values of $\Delta\Omega$. Each vortex grows in size when the stress is increased until a point is reached where the mode is no longer stable. A transition to a new mode with symmetry m' ($m' < m_c$) will occur. Section 5 will be devoted to the description of the range of stability of the successive modes m, to the

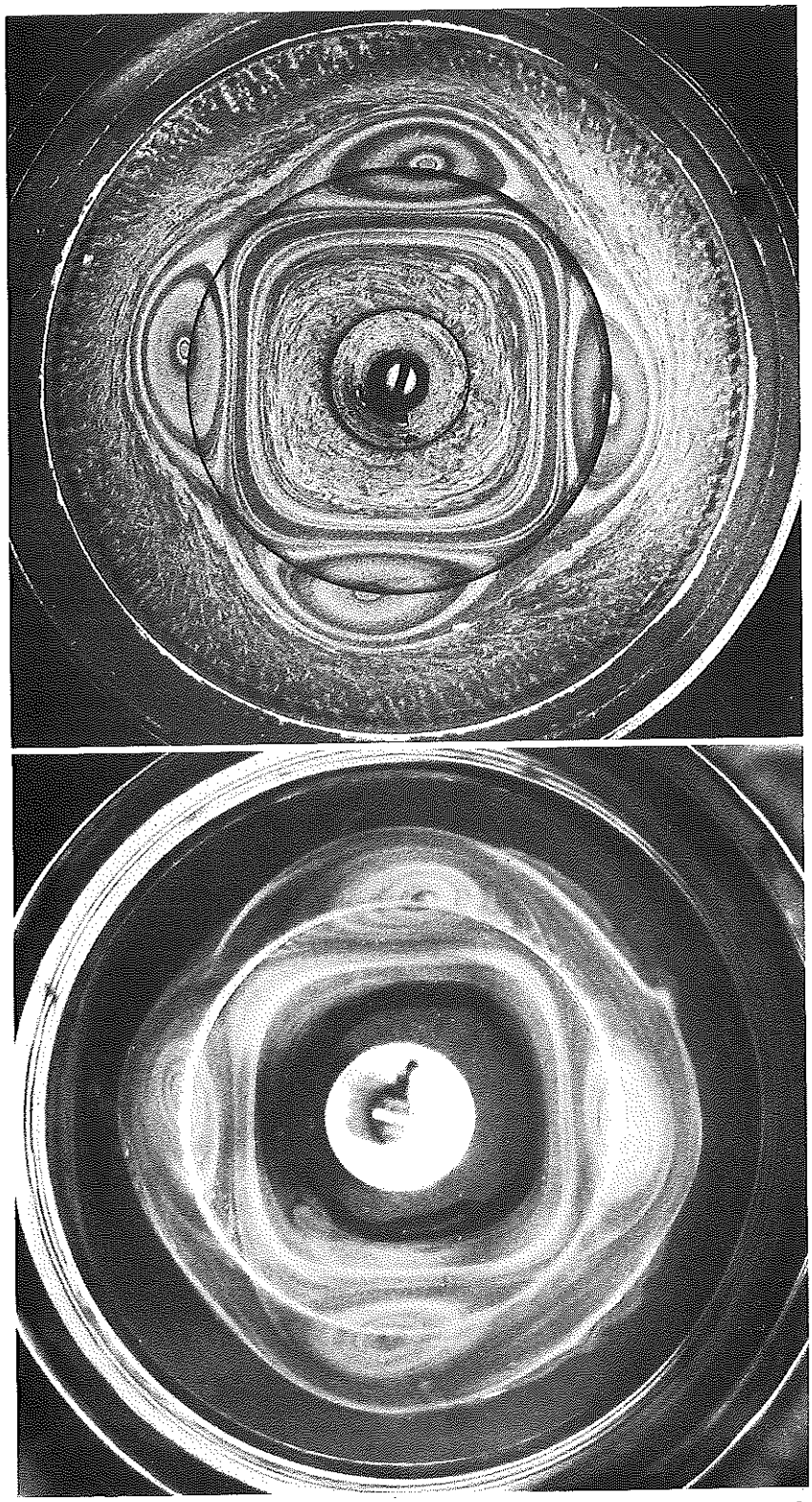

(a)

(b)

FIGURE 4. A mode $m = 4$ ($R_1 = 3$ cm, $e = 0.5$ cm, $\Omega_1 = -5.6$ rad/s, $\Omega_2 = 4.7$ rad/s) as observed: (a) with a soap film; (b) with smoke.

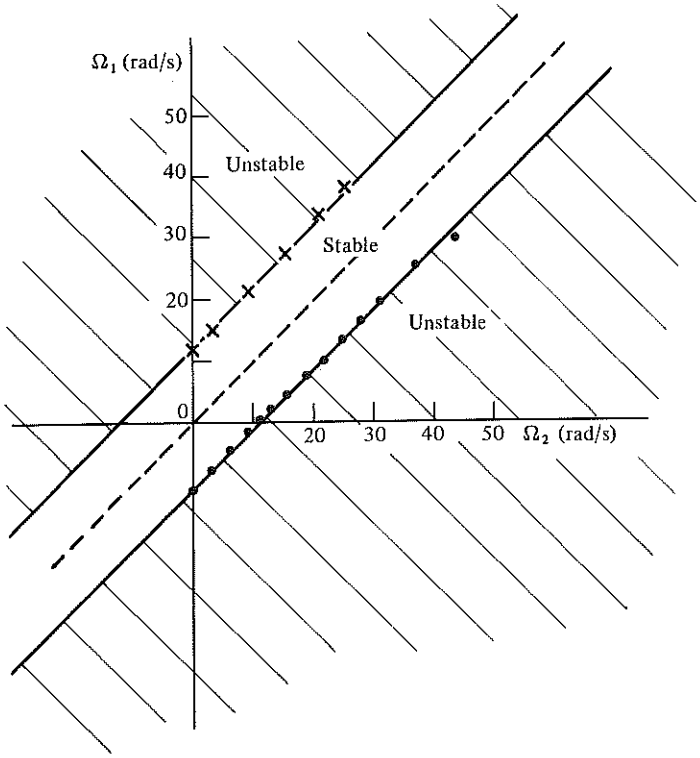

FIGURE 5. Measured angular velocities at the onset of the instability in the geometry $R_1 = 3$ cm; $e = 0.3$ cm.

	$\Delta\Omega_c$ (rad/s)	R_1 (cm)		
		2.1	3.0	4.0
e (cm)	0.2	30.7	21.3	17.8
	0.3	20.7, 18.2	13.8, 10	10.7, 7.5
	0.5	12.2, 10.7	8.2, 6.3	6.6, 6.3
	0.9	9.1, 9.4	5.6, 5	5.3, 5

TABLE 1. Critical values of the angular-velocity difference as a function of radius and thickness of the cell. In each case the first number is obtained by observation of the smoke, the second with the film.

where ν is the kinematic viscosity of air. For the smaller values of e (0.2, 0.4 and 0.5 cm) a critical value $Re_c \approx 85 \pm 5$ is found for the appearance of vortices observed with smoke. For $e = 0.9$ cm, we find $Re_c \approx 110 \pm 10$.

Observed with a film, the critical $\Delta\Omega_c$ are lower, but similar values of Re_c will be found if a correction is applied to take into account the resultant viscosity of both fluids enclosed in the cell.

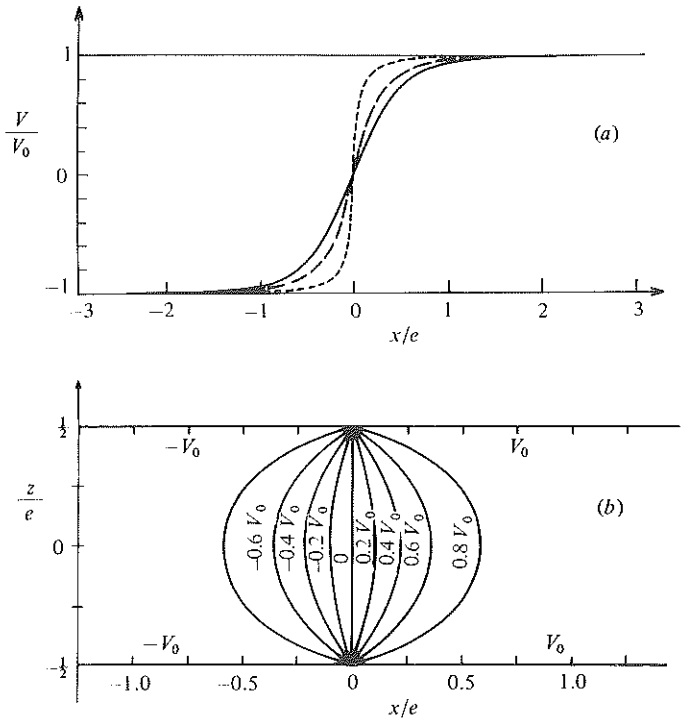

FIGURE 7. Velocity distribution of the laminar flow in the linear model. (*a*) Variation of the velocity along Ox for three values of z. ——, $z = 0$; — — —, $z = \pm 0.15e$; – – – –, $z = \pm 0.45e$. (*b*) Lines of equal velocities in the plane xOz (with linear dimensions normalized to e).

Taking into account that translational symmetry imposes $\partial p/\partial y = 0$, the system reduces to

$$\Delta v = 0.$$

The flow is symmetrical with reverse velocities on both sides of the plane $x = 0$. We will look for a solution on the $x > 0$ side, and impose the following boundary conditions:

$$v = 0 \quad (x = 0),$$

$$v = V_0 \quad (z = \pm \tfrac{1}{2}e \quad \text{or} \quad x = L).$$

The velocity field could be obtained by a Fourier expansion, but this would converge slowly due to the discontinuities in the boundary conditions.

Let

$$Z = (z + \mathrm{i}x)\, e^{-1}.$$

In the limit $L \to \infty$, a conformal transformation (Kober 1957) transforms the surface between $z = \pm \frac{1}{2}e$ and $x > 0$ into a half-plane limited by a straight line where we can solve $\Delta v = 0$.

Returning to the initial space, we find a velocity field

$$v(x, z) = (\operatorname{sign} x)\, V_0 \left[\frac{1}{2} + \frac{1}{\pi} \arctan \left(\frac{\operatorname{sh}^2 \dfrac{\pi x}{e} - \cos^2 \dfrac{\pi z}{e}}{2 \operatorname{sh} \dfrac{\pi |x|}{e} \cos \dfrac{\pi z}{e}} \right) \right].$$

Figure 7 (*a*) shows several computed $v(x)$ curves for different values of z. The map of equal values of v in the plane zOx is shown on figure 7 (*b*). Changing e changes the scale of the sketch but does not change the velocity profile, which is also independent of the value of the viscosity. However, the width $\delta(z)$ of the shear zone is a nearly parabolic function of z:

$$\frac{\delta(z)}{e} \approx 4\left(\frac{z}{e}+\frac{1}{2}\right)\left(\frac{1}{2}-\frac{z}{e}\right),$$

which has a maximum for $\delta(z=0) \approx e$.

4.4. *The threshold of the instability*

The Kelvin–Helmholtz instability affects the interface separating two fluids in parallel motion with different velocities. The simple use of the Bernouilli theorem shows that a perturbation affecting the interface will be amplified by the resulting change in local pressures. In the present experiment, we must compare this effect to the stabilizing effect of viscous friction on the walls.

The linear analysis of the Kelvin–Helmholtz instability, first given by Lord Rayleigh, can be found in Chandrasekhar (1961). We will use here the model in which the actual basic velocity profile is replaced by a linear variation of the velocity over a width δ (figure 8*a*). We will choose the tangent to the real profile in $x = 0$ and we will call $\delta(z)$ the width of the shear zone in a plane z (it depends quadratically on z). In this plane, the growth rate of a perturbation (in the Ox direction) characterized by its wavevector k would then be

$$\sigma' = \frac{V_0}{\delta(z)}[\mathrm{e}^{-2k\delta(z)} - (1-k\delta(z))^2]^{\frac{1}{2}},$$

which has a maximum (figure 8*b*)

$$\sigma_c = 0.4\frac{V_0}{\delta(z)} \quad \text{for} \quad k\delta(z) = 0.8.$$

This rate must be corrected. The basic flow is parallel to Oy. Any transverse component of the velocity, if created, is opposed by the friction on the horizontal walls (which is also responsible for variation of the shear width with z) and decreases exponentially with a characteristic lifetime τ. It corresponds in a plane z to a damping factor $1/\tau(z)$ which is the result of the friction on both walls of height $z_\omega = \pm\frac{1}{2}e$. Its order of magnitude is

$$\frac{1}{\tau(z)} = \frac{1}{\tau_1}+\frac{1}{\tau_2} = \nu\left(\frac{1}{(z-\frac{1}{2}e)^2}+\frac{1}{(z+\frac{1}{2}e)^2}\right).$$

The instability that will create such transverse components of the velocity can only develop if its growth rate $\sigma_c(z)$ is larger than $1/\tau(z)$:

$$0.4\frac{V_0}{\delta(z)} > \nu\left(\frac{1}{(z_0-\frac{1}{2}e)^2}+\frac{1}{(z_0+\frac{1}{2}e)^2}\right),$$

where $\delta(z)$ is the width of the shear in the plane z:

$$\delta(z) \approx \frac{4}{e}\left(\frac{e}{2}-z\right)\left(\frac{e}{2}+z\right).$$

This condition is easiest to satisfy in the median plane $z = 0$, which is thus the most-unstable region of the cell. There the instability starts growing for $Re_c = 2V_0\delta(0)/\nu \approx 40$, its wavevector is $k_c \approx 0.8/e$. The marginal stability curve is shown on figure 8 (*c*).

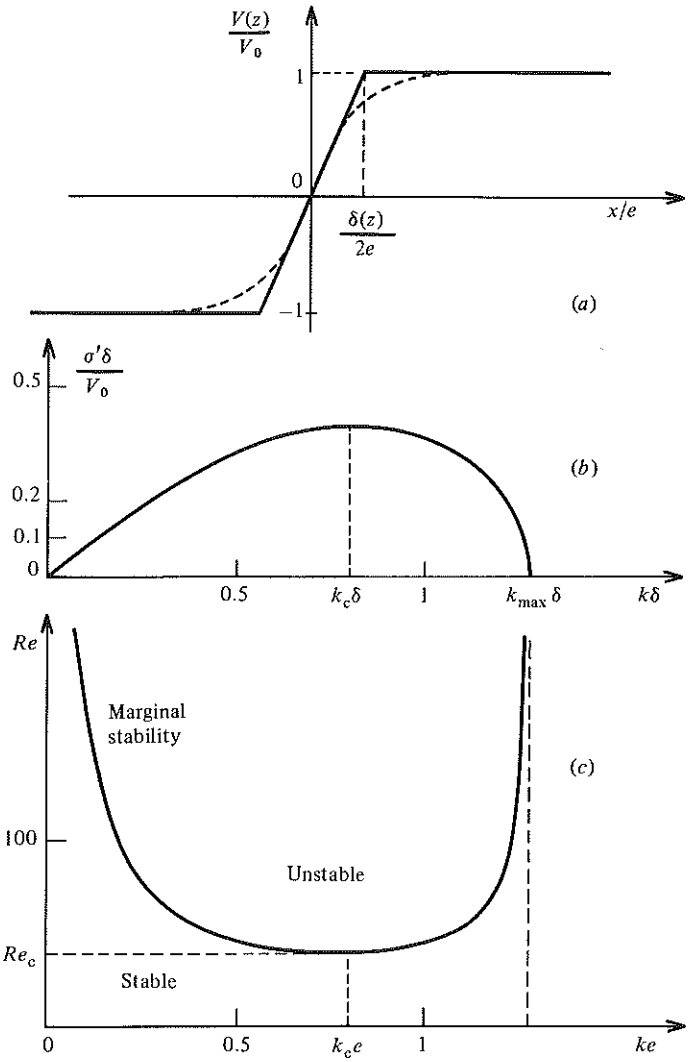

FIGURE 8. (*a*) Velocity distribution in a plane $z = Cte$ (– – –) and the modelling linear variation (——). (*b*) Growth rate σ' of a perturbation as a function of its wavevector k in the absence of friction on walls. (*c*) Marginal stability curve.

4.5. *Discussion and comparison with the experimental results*

A basic flow similar to the linear case would not be strictly a solution of the cylindrical Navier–Stokes equations. The velocity field cannot, then, be plane everywhere in the cell, and it is necessary to introduce components u_r and u_z to the velocity. No analytical solution can be found for this problem.

The linear model suggests that a Kelvin–Helmholtz instability would start growing in the median plane of the cell. There, for symmetry reasons, we now have

$$u_z = 0, \quad \frac{\partial(r u_\phi)}{\partial z} = 0, \quad \frac{\partial u_r}{\partial z} = 0.$$

$\partial u_z/\partial z$ is not necessarily zero, but u_z must be zero in the planes $z = \pm\frac{1}{2}e$ and $z = 0$.

If e is small, u_z is small everywhere and so is its derivative $\partial u_z/\partial z$ in the median plane. So an approximately two-dimensional motion is maintained in this region.

More generally, a first approximation of the flow in the cell is obtained when R_1 is large and Ω_1 and Ω_2 small, by using the following correspondence with the linear model

$$ru_\phi(r,z) \leftrightarrow v(x,z), \quad \Omega_1 R_1 \leftrightarrow -V_0, \quad \Omega_2 R_1 \leftrightarrow V_0.$$

In the linear geometry, we have given a qualitative treatment of the destabilization of the fluid planes $z = z_0$ treated independently. The pattern of vortices, as it appears experimentally, is characterized by a critical wavevector ($k_c \sim 0.85/e$) close to the predicted value in the median plane of the cell ($0.80/e$). It confirms that this is the region where the instability starts growing.

The model predicts a lower limit for Re_c corresponding to the plane $z = 0$: $Re_c(z = 0) = 40$. The destabilization of planes $z \neq 0$ requires larger values of Re_c. We observe $Re_c \approx 85$. A quantitative treatment of the appearance of the wave in the whole cell, taking into account the z-dependence of its amplitude, remains to be done and would lead to better predictions.

5. The vortex patterns

5.1. *Range of stability. Evolution of the wavevector*

The mode that appears at the onset will persist indefinitely if the velocities creating the shear constraint are maintained constant. If they are increased slowly, the size of each vortex will increase and the mode m_c will stay regular in a certain range. Then a disturbance will break the m_c-fold symmetry, leading to pairing of vortices and transition to a mode with $m' < m_c$.

The transitory phenomena will be described separately in §6. We will now study the selection of the modes and their range of stability.

Figure 9 shows the evolution of m when the Reynolds number is increased from 0 to 500, then decreased from 500 to 0 (in a geometry where $R = 3$ cm and $e = 0.3$ cm). When the increase is quasistatic, the observed transitions are successively $m_c \to m_c - 1$, then $m_c - 1 \to m_c - 2$. (The mode with the largest wavelength that can be reached in our geometry is $m = 2$.) During the decrease, the reverse phenomena will be observed with successive transitions $m \to m + 1$. Strong hysteresis effects are found at each of these transitions.

The total range of stability of a given mode (figure 10) will be bounded by the Reynolds value Re_{max} at which a transition to $m - 1$ occurs during the increase and by Re_{min} at which it will undergo a transition to $m + 1$ during the decrease.

In order to generalize these results, we compare the range of stability of a pattern of wavevector k (expressed in units $1/e$) obtained for different values of R_1 and e. A plot (figure 10) of Re_{max} and Re_{min} for observed values of ke in two different geometries show the coherence of the results. Two empirical laws can be deduced from the results:

$$ke \propto Re_{max}^{-0.6 \pm 0.1}, \quad ke \propto Re_{min}^{-1.5 \pm 0.3}.$$

The marginal stability curve is also shown on figure 10 as obtained theoretically and fitted by replacing the predicted value $Re_c \approx 40$ by the observed one $Re_c \approx 80$.

At present, no theory exists on the behaviour of the instability far from its threshold. However, the stability of linear chains of vortices has been investigated theoretically with model vortices of different types. A line of punctual vortices is always unstable and so is a line of vortices of the Stuart model (Pierrehumbert &

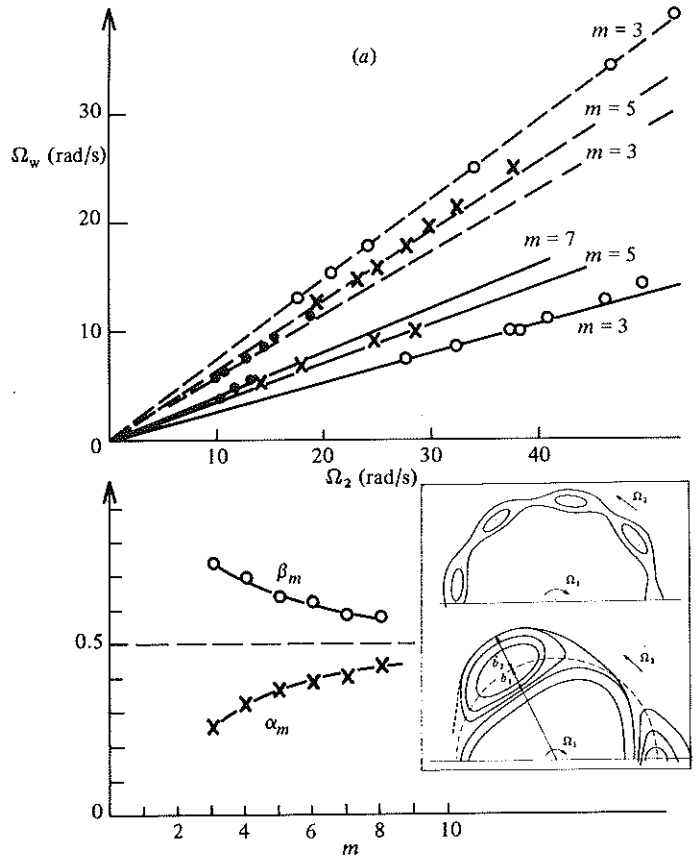

FIGURE 11. (*a*) Angular velocity of the vortices in three different patterns with $m = 3$, 5 and 7 as a function of Ω_2 with $\Omega_1 = 0$ (top curves) and as a function of Ω_1 with $\Omega_2 = 0$ (lower curves). $R_1 = 3$ cm; $e = 0.3$ cm. (*b*) The evolution of α_m and β_m as a function of m. (*c*) Shape of the vortices for large values of m and small values of m.

m	3	4	5	6	7	8
α_m	0.27	0.32	0.36	0.39	0.41	0.44
β_m	0.74	0.7	0.65	0.63	0.59	0.58
α_m^t	0.27	0.33	0.38	0.40	0.43	0.44
β_m^t	0.73	0.67	0.62	0.60	0.57	0.56

TABLE 3. Measured values of the coefficients α_m and β_m (the precision is 0.01) and corresponding values α_m^t and β_m^t predicted from the vortex shapes measured on photographs (the precision is 0.02)

The coefficients α_m^t and β_m^t of Ω_1 and Ω_2 satisfy

$$\alpha_m^t + \beta_m^t = 1.$$

Measurements of the values of b_1, b_2 and R_1 made on several photographs give values of α_m^t and β_m^t in good agreement with the experimental values (table 3).

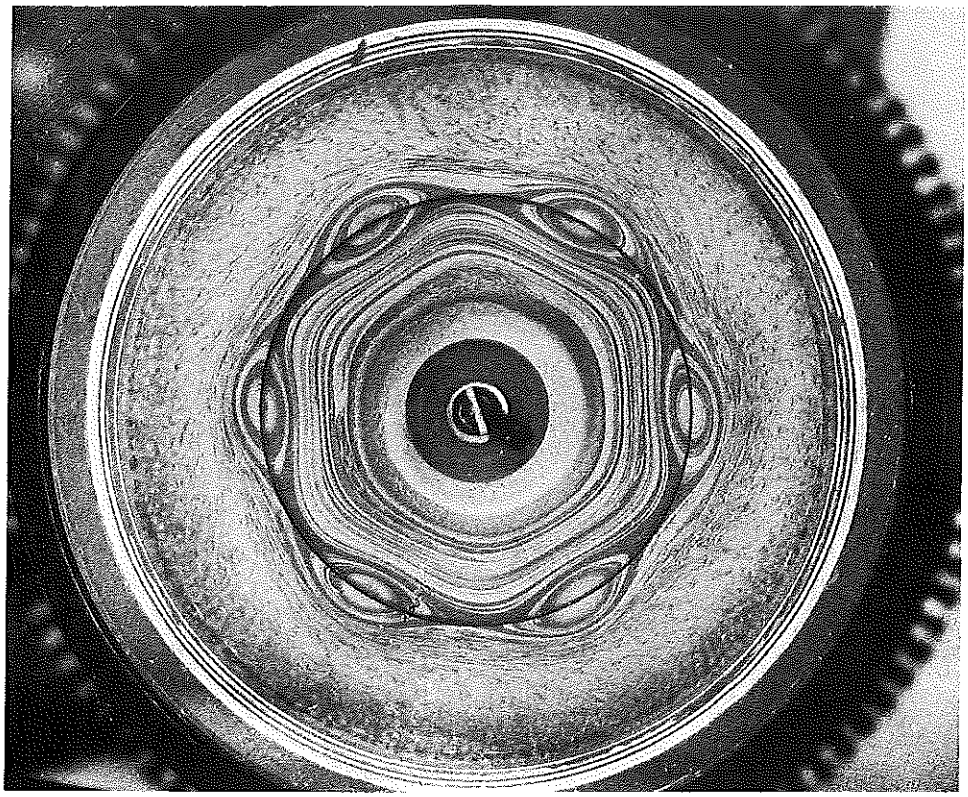

FIGURE 12. A regular $m = 6$ mode; $R_1 = 3$ cm, $e = 0.3$ cm, $\Omega_1 = -7.9$ rad/s, $\Omega_2 = 5.6$ rad/s.

6. The transitions between modes

The evolution of the wavevector with the Reynolds numbers imposes transitions between modes. In this chapter, we describe the transitory phenomena in terms of symmetries.

6.1. *Transitions under an increasing constraint*

Two distinct phases characterize the transition from one mode to the other $m \to m'$ $(m' < m)$.

The first phenomenon is the disappearance of the m-fold symmetry of the mode, and the formation of an intermediate state. This state is stable in a narrow range of values of the Reynolds number. Then, the transition itself will occur through the coalescence of one or several pairs of vortices. We will describe separately the transition process from initial modes with m of even and odd parity.

6.1.1. *Transition from a mode of even m*

A pattern of even m will progressively lose its initial symmetry as the amplitude of the vortices becomes modulated by a subharmonic wave of wavelength 2λ:

$$2\lambda = \frac{2\pi R_1}{\frac{1}{2}m}.$$

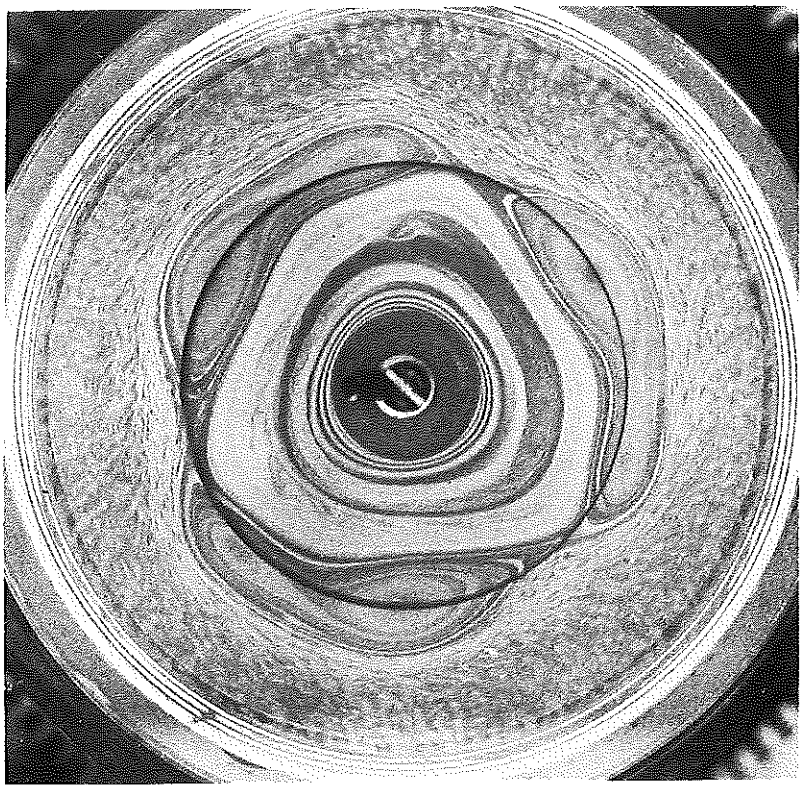

FIGURE 13. A mode $m = 6$ modulated with subharmonic spatial periodicity before transition to $m = 3$. Same geometry as figure 14. $\Omega_1 = -11.3$ rad/s clockwise, $\Omega_2 = 7.1$ rad/s anticlockwise.

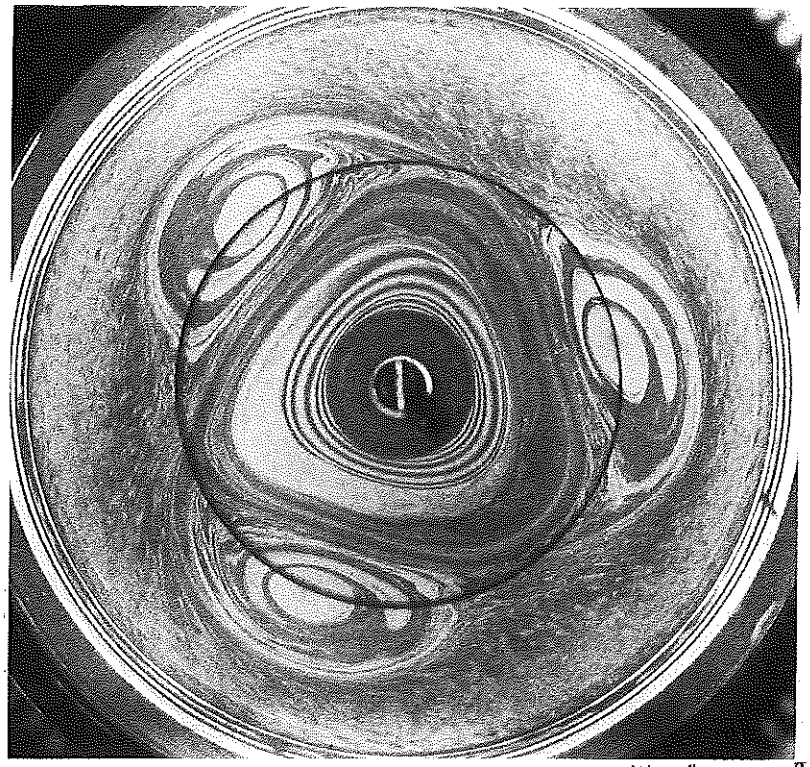

FIGURE 14. The appearance of the mode $m = 3$ after a transition from $m = 6$; $\Omega_1 = -13.3$ rad/s, $\Omega_2 = 8.65$ rad/s.

The m-fold symmetry is replaced by a $\frac{1}{2}m$ symmetry. The pattern has a stationary form in time. This phenomenon was observed for $m = 10, 8, 6, 4$, and is shown on figure 12 and 13, for $m = 6$. In the narrow range in which this intermediate mode is stable, the amplitude of the modulation increases with the stress. The position of the core of a small vortex becomes unstable under the influence of the velocity field of the two neighbouring large ones. It could be displaced either both forward (in the direction of Ω_1) and radially inward near the preceding vortex, or both backward and outward near the following one. Experimentally, only the second situation is observed (figure 13). Then, two evolutions are possible. If the acceleration is large enough, $\frac{1}{2}m$ pairings occur, each small vortex being caught up by the following large one and absorbed in a rotation around it.

The pattern then becomes a regular $\frac{1}{2}m$ type (figure 13 and 14). If the acceleration is small, only one pairing occurs and the other vortices become equal in size again and a regular $m-1$ mode is stabilized.

6.1.2. *Transition from a mode of odd m*

The visual observation in this case is more difficult. After the initial destabilization of the regular mode m, no geometrical symmetry is left in the intermediate state, and a general vacillation affects the amplitude of all the vortices (figure 15). However, a careful study of videotape recordings permits an analysis of the phenomenon which is similar for $m = 3, 5$ and 7. We will describe it in the rotating reference frame. During their vacillation, the vortices all go through amplitude and position oscillations. We will now number the vortices and take as the origin a vortex no. 1, which is smallest at time $t = 0$. A time τ later, the vortex no. 3 will be smallest and the general pattern will be identical with what it was at $t = 0$ but tilted by an angle $\theta = (2/m)\,(2\pi)$. At a time $m\tau$, the pattern will be identical with the initial state at $t = 0$.

This behaviour can be understood if we remark that, in the case of odd m, the subharmonic wavelength $2\pi R_1/\frac{1}{2}m$ is not quantized around the circle and thus cannot be excited. The nearest quantized spatial period is $\lambda' = 2\pi R_1/\frac{1}{2}(m+1)$. The observed patterns correspond to the basic mode m modulated by a wave of this wavelength λ' with an angular velocity

$$\omega' = \frac{\lambda'/R_1}{m\tau} = \frac{2\pi}{m\frac{1}{2}(m+1)\tau}$$

in the direction of Ω_2. The direction is probably due to the type of displacement of a small vortex in interaction with its neighbours as described previously. A simulation shown on figure 16 gives the aspect of the amplitude modulation of the vortex line at times $0, \tau, \ldots, m\tau$.

The vortices are also longitudinally displaced by the oscillation but this has not been included in the model of figure 16.

Ultimately, one pairing will usually take place and a transition to a mode $m-1$ will occur.

The spatiotemporal structure of the modulated state for both parities of m can be described in another way. Rand (1982) gave a mathematical classification of the modulated waves in rotating fields. He introduced three numbers (m, s, n). m is the order of the symmetry of the basic wave, s the order of symmetry of the modulated pattern; if τ is the minimum time for the pattern to be identical with an initial state, it has then been shifted by an angle $\theta = 2\pi n/m$, which defines n.

In this classification, when m is even we observe $(m, \frac{1}{2}m, 0)$, when m is odd $(m, 1, 2)$.

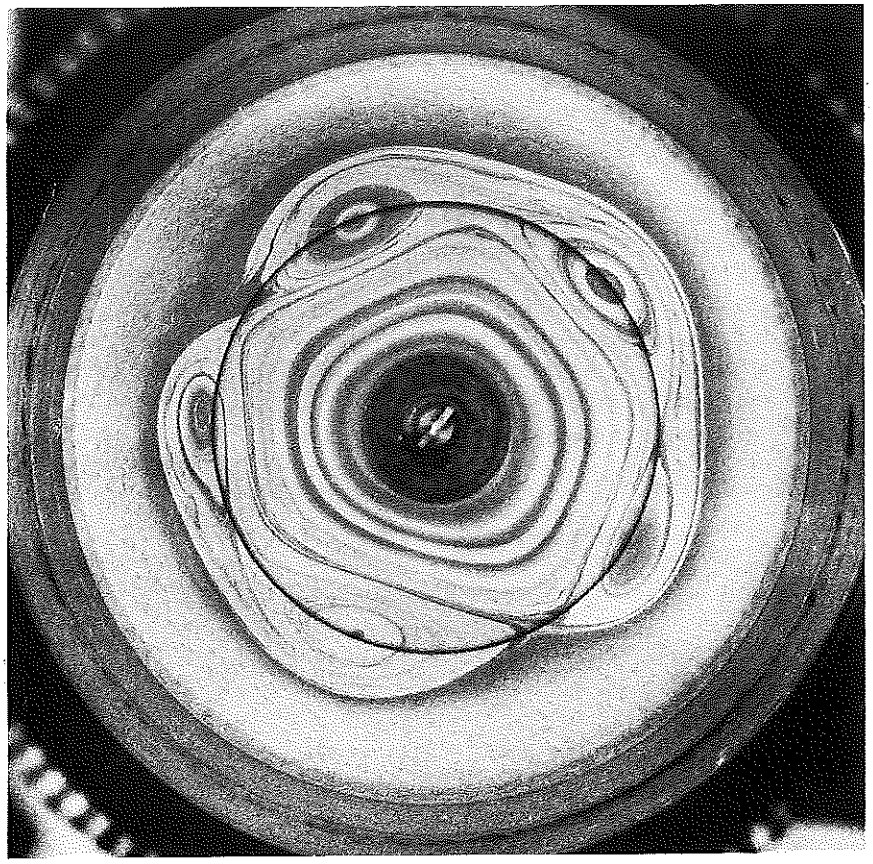

FIGURE 15. A modulated $m = 5$ pattern; $R_1 = 3$ cm, $e = 0.3$ cm, $\Omega_1 = -8.8$ rad/s, $\Omega_2 = 14.5$ rad/s.

6.2. *Transitions under decreasing stress*

The return transitions $m \to m'$ ($m' > m$) have a very different form. With the decrease of the shear stress, the vortices retain length but become slimmer. Then, a slow elliptic motion affects their core along the shear zone. The frequency of this motion decreases with decreasing stress. When the dimensions are such that a ratio $(b_1+b_2)/\lambda \sim 0.15$ is reached, the vortex splits with the appearance of a second core (figure 17). The phenomenon affects all the vortices, but a correlation between their oscillation was difficult to measure. The transitions $m \to m+1$ correspond to Reynolds numbers close to each other (see figure 9). The decrease has to be very slow to produce transitions $m \to m+1$, otherwise any transition from $m \to m+1$ to $m \to 2m$ can be observed.

6.3. *Transitions due to lateral friction*

When the external radius R_2 of the cell is not large enough compared with R_1, a specific phenomenon is observed. If the previous evolution of the wavenumber has led to a mode $m = 4$, for instance, which we will suppose stationary in the laboratory frame, a further increase of the stress will make the transverse dimension b_1+b_2 of the vortices grow larger, and friction on the lateral wall becomes important. The mode is no longer stable, and all vortices split simultaneously into two. In a transitory state,

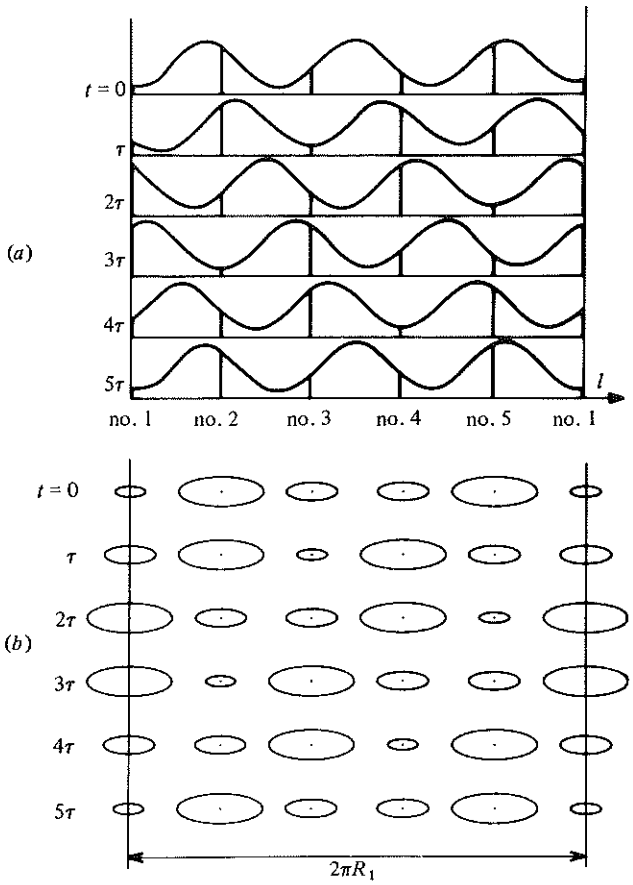

FIGURE 16. (*a*) The near-subharmonic wave that modulates the vortices amplitude in the case $m = 5$. It is represented at all the times at which similar but tilted patterns are observed. (*b*) Unrolled model of the observed amplitude modulation of the vortices.

eight little vortices will be present (figure 18), four of them moving forward and four backward. When they meet, they coalesce again into a $m = 4$ state identical with the initial one but tilted at an angle $\frac{1}{4}\pi$. This state is itself transitory and will split again. These relaxation oscillations are regular and their period has a linear dependence with $|\Omega_1 - \Omega_2|$. The same phenomenon is observed if a central cylinder is introduced in the cell, creating friction on the inner side.

7. Two limiting cases at large Reynolds numbers

The study of the further evolution of the flow for larger Reynolds numbers is beyond the scope of the present article. Re depends on Ω_1, Ω_2, R_1 and e. We will describe here two limiting cases where the structure of the flow changes.

(i) A specific type of flow appears in the experiments where both e is large and $|\Omega_1| \gg |\Omega_2|$. We have already noticed that the Re_c value observed for $e = 0.9$ cm was abnormally large. Observation with smoke reveals a three-dimensional structure of the flow. The Ekman-layer thickness of the central disks becomes in this case much smaller than e. Destabilization of the fluid by centrifugal action near the edges of the disks then creates two toroidal structures symmetrical with respect to the median

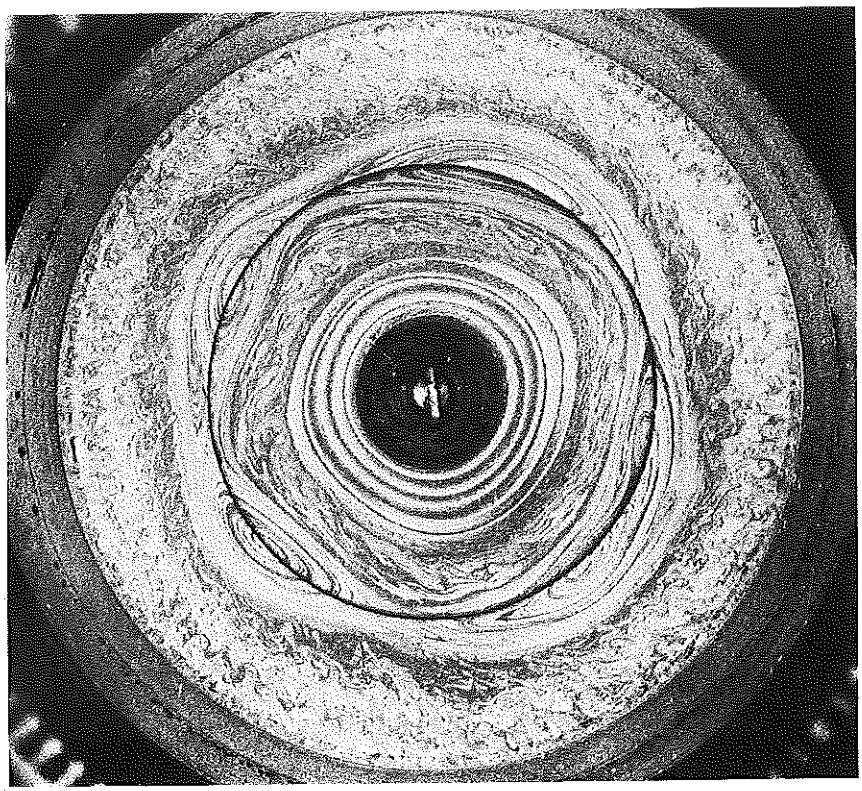

FIGURE 17. Splitting of vortices due to a decrease of the constraint. The initial mode was $m = 3$, successive splittings gave $m = 6$. Three different phases of the splitting can be seen on this photograph. The vortex at the top is elongated by the decrease of the stress. The vortex on the right is in the process of splitting. This splitting has already been completed on the left of the photograph.

plane. The appearance of the vortices in the central plane creates spiral folds of the tori (figure 19*a*, *b*).

(ii) Another phenomenon can be observed in the cells with a thickness e of the order of magnitude of the radius R_1. There the vortices start interacting directly through the central region (provided the axis R_0 has been removed). Each vortex is then in the velocity field created by all the others. The saddle points that separate neighbouring vortices along the shear zone move towards the centre of the cell. Their meeting (in the case $m = 3$) is shown on figure 20. For a larger stress they cross the central area and move towards the opposite side of the cell.

This evolution of the pattern has a remarkable analogy with the evolution of the Poincaré sections of Hénon's attractor (1969) when the control parameter is changed. It seems that this analogy of forms in two totally different spaces has a topological origin. In the Hénon attractor, when the system is Hamiltonian, the section is an area-preserving mapping. We have motions with div $\boldsymbol{v} = 0$ in two dimensions; the two conditions are similar and seem to lead to archetypal shapes.

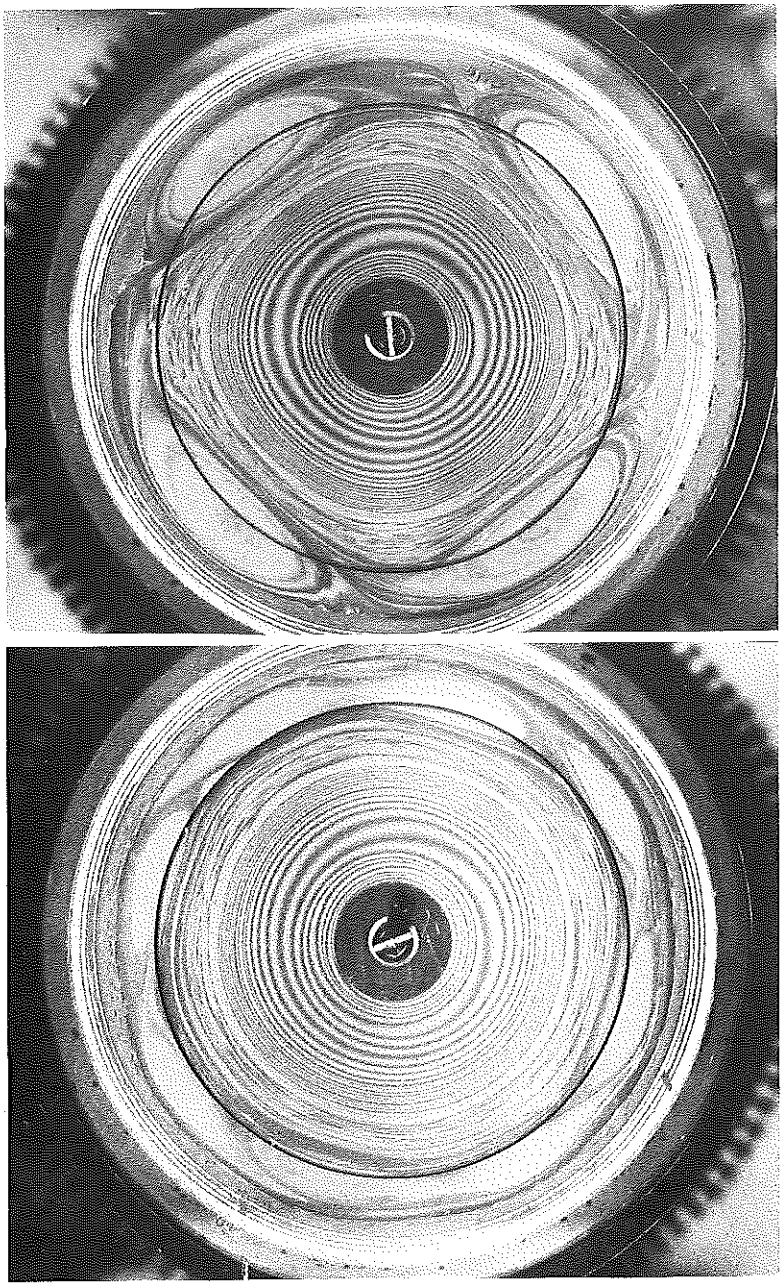

FIGURE 18. Oscillation between a mode $m = 4$ and a mode $m = 8$ due to friction on the lateral wall; $R_1 = 4$ cm, $R_2 = 5.1$ cm, $e = 0.9$ cm, $\Omega_1 = -14.8$ rad/s, $\Omega_2 = 4$ rad/s.

8. Concluding remarks

In summary, the results show that it is possible, if the previously discussed conditions are met, to obtain steady states of the shear flow instability in a circular geometry. The state of the flow is defined by a Reynolds number which compares the destabilizing effect of the shear stress with the damping due to viscous friction on the walls. This Reynolds number can thus be controlled by the externally imposed

thick corresponding to $\Gamma_0 \mu_s \approx 5 \times 10^{-6}$ surface P. In its motion parallel to the film, the air exerts friction on large surfaces. This force is only resisted by the viscous forces in the thin section of the film. In all our experiments, the lengthscale L of the horizontal velocity variation near the film is such that

$$L^2 \mu_{\text{air}} \gg Lt\mu_f \Rightarrow L \gg 2 \times 10^2 t.$$

In these conditions, the film is easily set into motion and follows exactly an air flow parallel to its surface.

If the air flow that interacts with the film is three-dimensional, the relation between its motion and the film motion will be complicated. The strong capillary forces will oppose any deformation of the plane and impose a $v_\perp = 0$ condition on its surface. The film is dragged by the air in the zones where the driving parallel velocity of the flow is the largest. Elsewhere, return currents appear in the film so as to maintain a divergence-free flow in its plane. The correspondence between the air flow and the observed motion of the film requires careful interpretation. (There is a similar problem in the relation between a three-dimensional flow in a liquid and the observed motions of a polluting layer on its free surfaces.)

If the air flow is two-dimensional and parallel to its surface, the film will follow its motion and provide several types of visualization.

(i) It is possible to observe the motion of suspended micelles on the film and thus to obtain the path of the particles.

(ii) The film, after its initial stretching, contains many patches of different thickness. These patches, when drawn into motion, get elongated and show the flowlines.

(iii) In the present experiment, the visualization is related to the drainage of the film due to its motion. It can be understood by comparison with the drainage of the soap films under the influence of gravity which was extensively studied by Mysels, Shinoda & Frenkel (1959). When a film is stretched on a vertical frame, after a few seconds a pattern of horizontal fringes alternately light and dark are observed in monochromatic light. They correspond to a continuous gradient of increasing thickness from the top to the bottom of the frame. Observation shows that a very slow drift of the fringes is due to the drainage of the film.

Mysels studied this phenomenon and classified three types of films with different drainage behaviour. Our films correspond to his mobile type. He showed that for these films marginal regeneration (suction of the film by the Plateau border) determines the rate of the thinning in rectangular frames. In the absence of this phenomenon (cylindrical films) the thinning is extremely slow because the motion due to the gravity forces is opposed by the internal viscous forces. During this drainage, the fringes are lines perpendicular to the driving gravity force.

In our system, we stretch a film on a horizontal circular frame. A rotation of the whole system will create in the film a series of concentric circular fringes corresponding to the thinning of the centre due to centrifugation. In the absence of marginal regeneration, the process of thinning is very slow.

When a non-axisymmetric flow appears, the drainage is due to the local centrifugal action eventually corrected by a Coriolis term. The centres of the vortices thin down and elliptical concentric fringes appear.

Finally, the drainage does not affect in return the general motion because of the difference in their velocity scales. While the imposed velocity field is of the order of several centimetres per second, the drainage has velocities three orders of magnitude smaller.

REFERENCES

BATCHELOR, G. K. 1967 *An Introduction to Fluid Dynamics*, pp. 177, 178. Cambridge University Press.

BUSSE, F. H. 1968 *J. Fluid Mech.* **33**, 577.

CHABERT D'HIERES, G. 1982 In *Proc. European Geophys. Soc., Leeds* (to be published).

CHANDRASEKHAR, S. 1961 *Hydrodynamic and Hydromagnetic Stability*, p. 481. Clarendon.

COLES, D. 1965 *J. Fluid. Mech.* **21**, 385.

COUDER, Y. 1981 *J. Physique Lett.* **42**, L429.

HÉNON, M. 1969 *Q. Appl. Maths* **27**, 291.

HIDE, R. & TITMAN, C. W. 1967 *J. Fluid Mech.* **29**, 39.

KOBER, K. 1957 *Dictionary of Conformal Representation*, p. 99. Dover.

MOORE, D. W. & SAFFMAN, P. G. 1969 *Phil. Trans. R. Soc. Lond.* A **264**, 597.

MOORE, D. W. & SAFFMAN, P. G. 1975 *J. Fluid Mech.* **69**, 465.

MYSELS, K. J., SHINODA, K. & FRANKEL, S. 1959 *Soap Films, Studies of Their Thinning*. Pergamon.

PIERREHUMBERT, R. T. & WIDNALL, S. E. 1981 *J. Fluid Mech.* **102**, 301.

PIERREHUMBERT, R. T. & WIDNALL, S. E. 1982 *J. Fluid Mech.* **114**, 59.

RAND, D. 1982 *Arch. Rat. Mech. Anal.* **59**, 1.

ROSHKO, A. 1976 *AIAA J.* **14**, 1349.

SIEGMANN, W. L. 1974 *J. Fluid Mech.* **64**, 289.

STEWARTSON, K. 1957 *J. Fluid Mech.* **3**, 17.

TRAPEZNIKOV, A. A. 1957 In *Proc. 2nd Intl Congress on Surface Activity*, vol. 1, p. 242.

WESKE, J. R. & RANKIN, T. M. 1963 *Phys. Fluids* **6**, 1397.

WINANT, C. D. & BROWAND, F. K. 1974 *J. Fluid Mech.* **63**, 237.